Strategy for tailoring the size distribution of nanospheres to optimize rough backreflectors of solar cells

STEFAN NANZ,[1,*] AIMI ABASS,[2] PETER M. PIECHULLA,[3] ALEXANDER SPRAFKE,[3] RALF B. WEHRSPOHN,[3,4] AND CARSTEN ROCKSTUHL[1,2]

[1]*Institute of Theoretical Solid State Physics, Karlsruhe Institute of Technology, 76131 Karlsruhe, Germany*
[2]*Institute of Nanotechnology, Karlsruhe Institute of Technology, 76021 Karlsruhe, Germany*
[3]*Institute of Physics, Martin Luther University Halle-Wittenberg, 06120 Halle (Saale), Germany*
[4]*Fraunhofer Institute for Microstructure of Materials and Systems, 06120 Halle (Saale), Germany*
[*]*stefan.nanz@kit.edu*

Abstract: We study the light-trapping properties of surface textures generated by a bottom-up approach, which utilizes monolayers of densely deposited nanospheres as a template. We demonstrate that just allowing placement disorder in monolayers from identical nanospheres can already lead to a significant boost in light-trapping capabilities. Further absorption enhancement can be obtained by involving an additional nanosphere size species. We show that the Power Spectral Density provides limited correspondence to the diffraction pattern and in turn to the short-circuit current density enhancement for large texture modulations. However, in predicting the optimal nanosphere size distribution, we demonstrate that full-wave simulations of just a c-Si semi-infinite halfspace at a single wavelength in the range where light trapping is of main importance is sufficient to provide an excellent estimate. The envisioned bottom-up approach can thus reliably provide good light-trapping surface textures even with simple nanosphere monolayer templates defined by a limited number of control parameters: two nanosphere radii and their occurrence probability.

References and links

1. S. Reber, M. Arnold, D. Pocza, and N. Schillinger, "ConCVD and ProConCVD: development of high-throughput CVD tools on the way to low-cost silicon epitaxy," Proceedings of the 24th European Photovoltaic Solar Energy Conference (2009). Hamburg, Germany.
2. T. Rachow, N. Milenkovic, B. Steinhauser, J. Benick, S. Janz, M. Hermle, and S. Reber, "Solar cells with epitaxial or gas phase diffused emitters above 21% efficiency," Energy Procedia **77**, 540–545 (2015).
3. H.-P. Wang, D.-H. Lien, M.-L. Lien, C.-A. Lin, H.-C. Chang, K.-Y. Lai, and J.-H. He, "Photon management in nanostructured solar cells," J. Mater. Chem. C **2**, 3144–3171 (2014).
4. S. Mokkapati and K. R. Catchpole, "Nanophotonic light trapping in solar cells," J. Appl. Phys. **112**, 101101 (2012).
5. C. Eisele, C. Nebel, and M. Stutzmann, "Periodic light coupler gratings in amorphous thin film solar cells," J. Appl. Phys. **89**, 7722–7726 (2001).
6. R. Dewan and D. Knipp, "Light trapping in thin-film silicon solar cells with integrated diffraction grating," J. Appl. Phys. **106**, 074901 (2009).
7. A. Abass, K. Q. Le, A. Alu, M. Burgelman, and B. Maes, "Dual-interface gratings for broadband absorption enhancement in thin-film solar cells," Phys. Rev. B **85**, 115449 (2012).
8. C. Rockstuhl, F. Lederer, K. Bittkau, and R. Carius, "Light localization at randomly textured surfaces for solar-cell applications," Appl. Phys. Lett. **91**, 171104 (2007).
9. S. Fahr, T. Kirchartz, C. Rockstuhl, and F. Lederer, "Approaching the Lambertian limit in randomly textured thin-film solar cells," Opt. Express **19**, A865–A874 (2011).
10. S. Jain, V. Depauw, V. D. Miljkovic, A. Dmitriev, C. Trompoukis, I. Gordon, P. V. Dorpe, and O. E. Daif, "Broadband absorption enhancement in ultra-thin crystalline Si solar cells by incorporating metallic and dielectric nanostructures in the back reflector," Prog. Photov. Res. Appl. **23**, 1144–1156 (2015).
11. M.-C. van Lare and A. Polman, "Optimized scattering Power Spectral Density of Photovoltaic Light-Trapping Patterns," ACS Photonics **2**, 822–831 (2015).

12. C. Trompoukis, I. Massiot, V. Depauw, O. E. Daif, K. Lee, A. Dmitriev, I. Gordon, R. Mertens, and J. Poortmans, "Disordered nanostructures by hole-mask colloidal lithography for advanced light trapping in silicon solar cells," Opt. Express **24**, A191–A201 (2016).
13. M. Kroll, S. Fahr, C. Helgert, C. Rockstuhl, F. Lederer, and T. Pertsch, "Employing dielectric diffractive structures in solar cells – a numerical study," Phys. Stat. Sol. (a) **205**, 2777–2795 (2008).
14. C. Rockstuhl, S. Fahr, and F. Lederer, "Absorption enhancement in solar cells by localized plasmon polaritons," J. Appl. Phys. **104**, 123102 (2008).
15. S. Pillai, K. R. Catchpole, T. Trupke, and M. Green, "Surface plasmon enhanced silicon solar cells," J. Appl. Phys. **101**, 093105 (2007).
16. C. Rockstuhl, S. Fahr, F. Lederer, K. Bittkau, T. Beckers, and R. Carius, "Local versus global absorption in thin-film solar cells with randomly textured surfaces," Appl. Phys. Lett. **93**, 061105 (2008).
17. M. A. Green and S. Pillai, "Harnessing plasmonics for solar cells," Nat. Photon. **6**, 130–132 (2012).
18. C. Battaglia, C.-M. Hsu, K. Söderström, J. Escarré, F.-J. Haug, M. Charrière, M. Boccard, M. Despeisse, D. Alexander, M. Cantoni, Y. Cui, and C. Ballif, "Light trapping in solar cells: Can periodic beat random?" ACS Nano **6**, 2790–2797 (2012).
19. M. Peters, C. Battaglia, K. Forberich, B. Bläsi, N. Sahraei, and A. G. Aberle, "Comparison between periodic and stochastic parabolic light trapping structures for thin-film microcrystalline silicon solar cells," Opt. Express **20**, 29488–29499 (2012).
20. P. Kowalczewski, A. Bozzola, M. Liscidini, and L. C. Andreani, "Light trapping and electrical transport in thin-film solar cells with randomly rough textures," J. Appl. Phys. **115**, 194504 (2014).
21. U. W. Paetzold, M. Smeets, M. Meier, K. Bittkau, T. Merdzhanova, V. Smirnov, D. Michaelis, C. Waechter, R. Carius, and U. Rau, "Disorder improves nanophotonic light trapping in thin-film solar cells," Appl. Phys. Lett. **104**, 131102 (2014).
22. A. Oskooi, P. A. Favuzzi, Y. Tanaka, H. Shigeta, Y. Kawakami, and S. Noda, "Partially disordered photonic-crystal thin films for enhanced and robust photovoltaics," Appl. Phys. Lett. **100**, 181110 (2012).
23. S. Wiesendanger, M. Zilk, T. Pertsch, C. Rockstuhl, and F. Lederer, "Combining randomly textured surfaces and photonic crystals for the photon management in thin film microcrystalline silicon solar cells," Opt. Express **21**, A450–A459 (2013).
24. S. Fahr, C. Rockstuhl, and F. Lederer, "Engineering the randomness for enhanced absorption in solar cells," Appl. Phys. Lett. **92**, 171114 (2008).
25. E. R. Martins, J. Li, Y. Liu, J. Zhou, and T. F. Krauss, "Engineering gratings for light trapping in photovoltaics: The supercell concept," Phys. Rev. B **86**, 041404(R) (2012).
26. E. R. Martins, J. Li, Y. Liu, V. Depauw, Z. Chen, J. Zhou, and T. F. Krauss, "Deterministic quasi-random nanostructures for photon control," Nat. Commun. **4**, 2665 (2013).
27. F. Priolo, T. Gregorkiewicz, M. Galli, and T. Krauss, "Silicon nanostructures for photonics and photovoltaics," Nat. Nanotechnol. **9**, 19–32 (2014).
28. X. Guo, D. Wang, B. Liu, S. Li, and X. Sheng, "Enhanced light absorption in thin film silicon solar cells with Fourier-series based periodic nanostructures," Opt. Express **24**, A408–A413 (2016).
29. R. Yu, Q. Lin, S.-F. Leung, and Z. Fan, "Nanomaterials and nanostructures for efficient light absorption and photovoltaics," Nano Energy **1**, 57–72 (2012).
30. X. Meng, V. Depauw, G. Gomard, O. E. Daif, C. Trompoukis, E. Drouard, C. Jamois, A. Fave, F. Dross, I. Gordon, and C. Seassal, "Design, fabrication and optical characterization of photonic crystal assisted thin film monocrystalline-silicon solar cells," Opt. Express **20**, A465–A475 (2012).
31. S. Wiesendanger, M. Zilk, T. Pertsch, F. Lederer, and C. Rockstuhl, "A path to implement optimized randomly textured surfaces for solar cells," Appl. Phys. Lett. **103**, 131115 (2013).
32. F. Pratesi, M. Burresi, F. Riboli, K. Vynck, and D. S. Wiersma, "Disordered photonic structures for light harvesting in solar cells," Opt. Express **21**, A460–A468 (2013).
33. T. Okamoto, K. Shinotsuka, E. Kawamukai, and K. Ishibashi, "Self-assembly method for controlling spatial frequency response of plasmonic back reflectors in organic thin-film solar cells," Appl. Phys. Express **10**, 012301 (2017).
34. T. Itoh and N. Yamauchi, "Surface morphology characterization of pentacene thin film and its substrate with under-layers by power spectral density using fast Fourier transform algorithms," Appl. Surf. Sci. **253**, 6196–6202 (2007).
35. C. Rockstuhl, S. Fahr, K. Bittkau, T. Beckers, R. Carius, F.-J. Haug, T. Söderström, C. Ballif, and F. Lederer, "Comparison and optimization of randomly textured surfaces in thin-film solar cells," Opt. Express **18**, A335–A342 (2010).
36. N. Sahraei, K. Forberich, S. Venkataraj, A. G. Aberle, and M. Peters, "Analytical solution for haze values of aluminium-induced texture (AIT) glass superstrates for a-Si:H solar cells," Opt. Express **22**, A53–A67 (2014).
37. S. J. Fonash, *Introduction to Light Trapping in Solar Cell and Photo-detector Devices* (Academic Press, 2015), 1st ed.
38. S. M. George, "Atomic Layer Deposition: An Overview," Chem. Rev. **110**, 111–131 (2010).
39. S. Wiesendanger, T. Bischoff, V. Jovanov, D. Knipp, S. Burger, F. Lederer, and C. Rockstuhl, "Effects of film growth modes on light trapping in silicon thin film solar cells," Appl. Phys. Lett. **104**, 231103 (2014).
40. J.-P. Berenger, "A perfectly matched layer for the absorption of electromagnetic waves," J. Comput. Phys. **114**, 185–200 (1994).

41. M. Green and M. Keevers, "Optical properties of intrinsic silicon at 300 K," Prog. Photov. Res. Appl. pp. 189–192 (1995).
42. Z. Holman, M. Filipic, A. Descoeudres, S. D. Wolf, F. Smole, M. Topic, and C. Ballif, "Infrared light management in high-efficiency silicon heterojunction and rear-passivated solar cells," J. Appl. Phys. **113**, 013107 (2013).
43. P. B. Johnson and R. W. Christy, "Optical constants of the noble metals," Phys. Rev. B **6**, 4370–4379 (1972).
44. K. Jäger, D. Linssen, O. Isabella, and M. Zeman, "Ambiguities in optical simulations of nanotextured thin-film solar cells using the finite-element method," Opt. Expr. **23**, A1060–A1071 (2015).
45. S. G. Romanov, S. Orlov, D. Ploss, C. K. Weiss, N. Vogel, and U. Peschel, "Engineered disorder and light propagation in a planar photonic glass," Sci. Rep. **6**, 27264 (2016).
46. J. Pomplun, S. Burger, L. Zschiedrich, and F. Schmidt, "Adaptive finite element method for simulation of optical nano structures," Phys. Stat. Sol. **244**, 3419–3434 (2007).
47. ASTM, "Standard tables for reference solar spectral irradiances: Direct normal and hemispherical on 37° tilted surface," (2012). West Conshohocken (PA): American Society for Testing and Materials. Available from https://www.astm.org.

1. Introduction

Thin-film silicon solar cells are being revisited by several groups and companies world-wide due to their better materials and energy efficiency and thereby possibly lower production cost. Whereas ten years ago, focus was mainly on PECVD-based microcrystalline technologies, nowadays, thin film crystalline solar cells are being prepared by high-throughput casting or high-temperature CVD processes [1, 2]. Thin-film cells can be made to be mechanically flexible and more portable. A thinner absorber layer also implies a shorter diffusion path for the generated minority carriers to reach the semiconductor junction, which in turn may translate to a better internal quantum efficiency (IQE) of the solar cell. However, for weakly absorbing materials such as c-Si, a thinner active material may lead to incomplete light absorption, which leads to a lower short-circuit current density [3, 4].

To address the incomplete absorption problem in thin-film devices, several possibilities have been proposed. Many approaches involve the usage of nanostructures which are either periodic [5–7] or random [8–12], placed at the back [13] or front side of the cell, or both [14]. These nanostructures enhance light absorption by improving light incoupling from air/glass superstrate to the higher-index absorber layer and also by increasing the effective light path within the absorber (light trapping). Metallic nanostructures have also been proposed for providing absorption enhancement by exploiting their various modes with strong scattering cross-section and large near-field enhancement [15–17]. However, with such lossy metallic structures there is also significant parasitic absorption, which leads to a lower absorption in the silicon layer.

Introducing disorder in light-trapping surface textures has been demonstrated to possibly lead to a spectrally broader absorption enhancement in photovoltaic devices [18–21]. Having disorder populates the Fourier spectrum of the geometry, which in turn leads to more available light scattering pathways across an extended spectral domain. However, not every disordered structure is equally useful as light absorption may instead be impaired [22]. Not just the availability, but also the scattering strength to the different pathways is important. Disorder may also enhance light scattering within the escape cone and may weaken with that the resonant optical response, resulting in less absorption enhancement. Therefore, obtaining the most out of disorder for light trapping purposes requires care and remains a major design challenge, especially due to huge computational costs in numerically addressing the problem. Furthermore, reliable large-area fabrication of optimum disordered light-trapping surface textures is highly demanding.

In an attempt to deduce and realize optimal light-trapping textures, many strategies have been explored. Among them is the combination of photonic crystal structures with disordered layers, e.g. using several layers with ordered and disordered structures [23]. Fahr *et al.* explored how statistical parameters that describe a surface texture can be tuned to ensure an optimal scattering pattern for absorption enhancement [24]. Martins *et al.* proposed a deterministic way to deduce an optimum quasi-periodic surface profile by superposing periodic gratings [25, 26]. Supercells resulting from several superposed grating periods may have a richer Fourier spectrum than single

periodic cells, thus providing a more broadband diffraction response while still retaining distinct diffraction orders [27, 28]. Though one can deduce with these approaches a favorable surface texture possessing the desired scattering response, the resulting textures are typically difficult to fabricate and often rely on relatively expensive top-down methods [29, 30].

Recently, a bottom-up strategy to define rough textures utilizing dielectric nanospheres with tailored radius sizes as building blocks has been proposed [31]. These nanospheres are grown in the liquid phase and the resulting colloidal dispersion is deposited onto a substrate. The properties of the solution and deposition method are tuned such that the deposited nanospheres form a monolayer on the substrate. This monolayer of nanospheres then defines a rough surface which serves as a template for a backreflector in solar cells. A similar approach with a disordered photonic crystal was already discussed [32]. There, they considered holes in a dielectric medium with correlated and uncorrelated positional disorder. Also, colloidal particles have been shown to enhance the absorption in organic thin-film solar cells [33].

Here, we demonstrate how favorable scattering properties for light trapping can be reliably obtained with the nanospheres-based bottom-up approach by utilizing nanospheres of only two different sizes. The resulting textures possess a Fourier spectrum that favors oblique scattering of normal incident light in a broad wavelength range, which in turn provides a large enhancement in absorption if the texture is an integrated part of a thin-film solar cell. This in turns yields an enhanced short-circuit current density when considering the full solar cell stack. One can hereby circumvent the need for full-wave simulations in a large parameter regime but still work towards optimizing the surface textures to be of use in thin-film solar cells.

For the analysis we use the well-known Power Spectral Density (PSD) [11, 34]. This quantity, which is the absolute square of the Fourier transform of the height profile, provides the amplitudes of the spatial frequencies, i. e. the grating vectors, that are available in the corrugated surface. It is hence a useful tool for our purposes in tailoring the nanosphere sizes via optimizing the amplitudes of the relevant grating vectors. Other measures such as the haze, which is basically the fraction of the specular and diffracted light, exist as well [35, 36], but they suffer from the inability to clearly distinguish the angular distribution and treat textures that scatter light into large oblique angles, which is generally favorable, comparable to textures that scatter the light into weakly oblique angles.

2. Strategy and simulations

2.1. General considerations

In this work, we consider the case of a simplified thin-film c-Si cell depicted in Fig. 1(a). We particularly discuss in this section the scattering properties we wish to achieve for an optimum light trapping rear-side texture. We also discuss how one can achieve a comparable response from textures obtained with the nanosphere-based bottom-up approach.

Before we proceed in discussing how to deduce nanosphere size distributions of interest, we first outline the desired scattering response that we aim to achieve. As the goal is absorption enhancement, one essentially seeks to utilize the disordered surface texture to scatter light into oblique angles within the light-absorbing medium [37]. For first order diffraction scattering processes, an incident wave with parallel wave vector $\vec{k}_{||,\text{inc}}$ will only be scattered to a certain mode $\vec{k}_{||}$ if the scattering texture height profile possesses a Fourier component with wavevector $\vec{G}$, fulfilling $\vec{k}_{||,\text{inc}} + \vec{G} = \vec{k}_{||}$. To significantly scatter (near) normal incident light to oblique angles via a first order diffraction scattering process, the surface texture must therefore possess Fourier components pertaining to sufficiently large $|\vec{G}|$. However, for the purpose of rear-side textures, height-profile Fourier components corresponding to $|\vec{G}| > k_0 n_{\text{Si}}$ can result in significant parasitic absorption losses as they facilitate scattering to plasmonic modes that are evanescent in the relevant spatial domain. These plasmonic evanescent modes may encompass strong
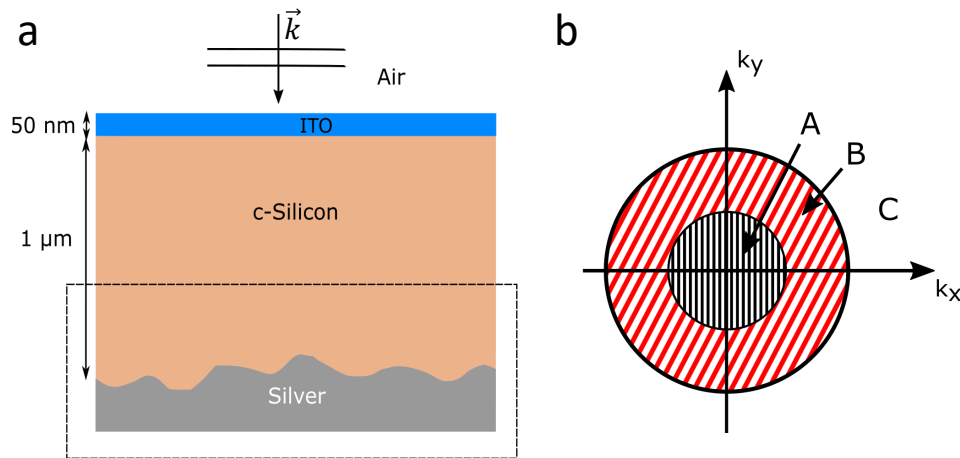
a

b

Fig. 1. a) A two-dimensional slice through the three-dimensional geometry of the considered thin-film solar cell used for full-wave FEM simulations with normal incident plane waves. Above the silver rough back-reflector whose height profile we are optimizing in this work, 1 μm of c-Si is considered. To reduce reflections at the front side, a 50 nm Indium tin oxide (ITO) anti-reflection layer is deposited on top of the silicon. The geometry in the dashed box was used for full-wave diffraction simulations, i.e. when calculating the angular spectrum. The entire three-dimensional geometry was considered when analyzing the short-circuit current density. b) To judge the quality of a rough surface, the Fourier spectrum was divided into three regions: A, for angles smaller than the angle of total internal reflection (TIR) at a silicon-air interface; B, for angles larger than the TIR angle, considering only propagating modes; C, evanescent wave vector components. We aim to tailor the diffraction spectrum to have its major contributions in region B.

parasitic absorption supported at the metal-dielectric interface that overshadows the absorption enhancement in the light absorbing media if one is not careful. Thus, our considerations above let us conclude that we require a height profile for our texture that possesses a Fourier spectrum as shown in Fig. 1(b), in which the Fourier distribution forms an annulus.

The outer and inner radius of the target annulus region are subject to optimization. The optimization requires to consider the intrinsic absorption response of the solar-cell material and the incoming solar irradiation. The Fourier spectra of a light trapping texture should be chosen in a way to account for the wavelength range where the absorption enhancement is most beneficial. For example, photons with energy significantly higher than the bandgap are already absorbed to a large extend within the first few hundred nanometers. In this wavelength regime, one only needs to ensure good anti-reflection properties of the front surface. Light trapping is most relevant for photons with energy close to the bandgap of the absorber, which experience a weak material absorption response. Although one should aim for the wavelength regime where a mere double pass through the absorber layer is not enough to ensure complete absorption, one should still prioritize the wavelength range where the solar spectrum offers the most photons.

Based on our discussion above, the main target wavelength region to enhance absorption is approximately 600–900 nm, for the case of thin-film c-Si cells. In order to provide a proof-of-principle demonstration of how one can design a light trapping structure for this wavelength regime, we aim to tailor the Fourier spectrum of our scattering surface in the shape of an annulus with the wavelength of 700 nm in mind. The inner radius of the target annulus distribution shall correspond to the angle of total internal reflection at a c-Si/air interface for this wavelength.
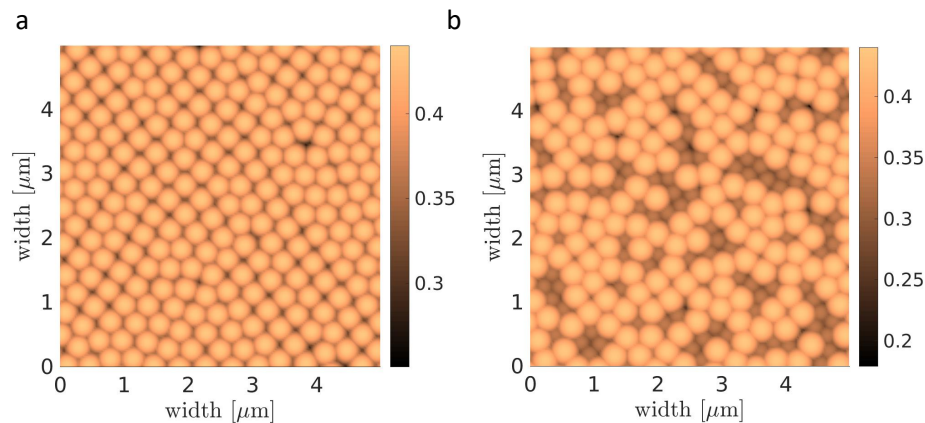
Fig. 2. a) Example monolayer consisting of nanospheres with only one radius (170 nm) and an isotropic coating layer with thickness 100 nm. Parts of the monolayer form a hexagonal pattern, whereas others are disordered. b) Example monolayer with 60 % of nanospheres with radius 170 nm and 40 % nanospheres with radius 120 nm. Again, a 100 nm thick isotropic layer has beed added. The small nanospheres lead to the vanishing of any remaining order of the bigger nanospheres.

For the outer radius, the largest propagating spatial frequency was chosen to avoid large losses through parasitic absorption in the metal.

2.2. Methodology

Having identified a target scattering characteristic, we proceed to investigate surfaces that can be obtained with a nanosphere-based bottom-up approach. In this work, we consider only nanosphere monolayers that are densely arranged, i.e. where neighboring nanospheres always touch each other, but nevertheless positional randomness is allowed. This constraint enables in principle a hexagonal close-packing of the nanospheres in the case of only one radius size, but also, and this is what we are focusing on here, a disordered monolayer. Surface textures arising from such monolayers are of particular interest as the statistical characteristics of the geometrical features would depend only on the nanospheres sizes and relative concentration of the nanosphere species. Though by doing so we restrict the degrees of freedom, the dense nanosphere monolayer distribution can provide a Power Spectral Density (PSD) distribution that approaches the target annulus profile distribution as will be shown below. Examples of monolayers using different nanosphere distributions can be seen in Figs. 2(a) and 2(b).

Our numerical height profile generation works as follows: We first generate a set of spheres with the desired radii in random order. The number of generated spheres is determined by the area of the box that we want to cover, ensuring that enough spheres are generated to cover the complete box, while also generating not too much to not distort the initialized nanosphere size distribution. The suitable number of nanospheres is different for different fractions of big and small nanospheres and determined individually for each configuration. We then initialize a random x-coordinate for each nanosphere while the initial y-coordinate is always set to the same value on one of the edges of the box. Then, the nanospheres are gradually moved towards the opposite side of the box until they either reach the opposite edge or touch another already placed nanosphere. After this, the nanosphere is moved along the x-direction to check if there is a position where it could be moved even further in y-direction to ensure uniform filling along the x-axis. The filling finishes when no not-deposited nanosphere is remaining or when the box
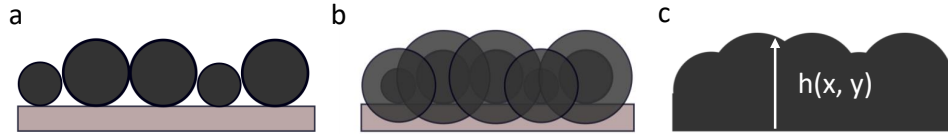
Fig. 3. Procedure to generate the rough surface template. Displayed is a two-dimensional cross-section of the three-dimensional height profile. a) Nanospheres are placed in a monolayer with the restriction that every nanosphere touches at least one other nanosphere. Overlapping nanospheres are not allowed. b) To mimic the isotropic coating by atomic layer deposition, the nanospheres are radially enlarged. c) The last step is to homogenize the resulting structure. The height profile is then the maximal height resulting from the enlarged nanospheres.

is full. For cases where too many nanospheres could not be placed in the box or the box was not filled, the result was discarded and restarted with an adapted number of nanospheres. A two-dimensional cross-section of such a nanosphere monolayer is shown in Fig. 3(a).

To build the surface texture template, the nanosphere monolayer is subsequently coated in an isotropic manner, which can be experimentally done via atomic layer deposition [38]. The isotropic coating thickness is chosen to be 100 nm to avoid texture smoothing, which would result in a decrease of surface amplitude and in turn would lead to weaker scattering [39]. Numerically, the isotropic coating can be deduced by first enhancing every nanosphere radially, as shown in Fig. 3(b). The final height profile can then be calculated by retrieving the continuous surface which is represented by the highest point of the enhanced nanospheres at each position (Fig. 3(c)). Since we are not interested in the zeroth order scattering strength, we set the average height of our profiles to zero. As a last step, we cut a small strip of the height profile on each side to avoid edge effects that encompass the placing process, and we apply a periodification to the height profile at the computational domain edges to be able to handle the scattering problem numerically; 50 nm on two adjacent sides of the height profile are modified in order to have a continuous transition to the next unit cell.

For the finite-element simulations, we place Perfectly Matched Layers (PMLs) in z-direction at the top and bottom of the computational domain to avoid unphysical reflections from the boundaries [40]. In the x-y-plane periodic boundary conditions are enforced. We simulate for p-polarized plane waves incident from the positive z-direction. The minimum and maximum finite-element degrees were chosen to be 2 and 3, respectively. The maximum mesh sidelength of the computational domain was 200 nm in the x-y-plane and varied along the z-axis for the different materials and also inside one material to ensure a sufficient fine mesh near the corrugated interface. We chose as maximum vertical mesh sizes 140 nm to 150 nm in silver, 50 nm to 80 nm in c-Si, 20 nm in ITO and 50 nm in air. The refractive indices for crystalline silicon [41], ITO [42], and silver [43] have been taken from published data.

2.3. *Tailoring scattering properties*

The simplicity in predicting the resulting height profile allows one to exploit knowledge of the scattering process in determining the nanospheres' size of interest. Along with the knowledge of the height profile, one has access to the Fourier picture of the geometry, which can be used to identify guidelines to deduce parameter regions of interest for the nanosphere compositions. One of the predictors of whether the scattering facilitated by a Fourier component with wavevector $\vec{G}$ is significant, is the PSD. The $\text{PSD}(\vec{G})$ is defined as the absolute square of the two-dimensional discrete Fourier transform of the height profile $h(x, y)$ [34],
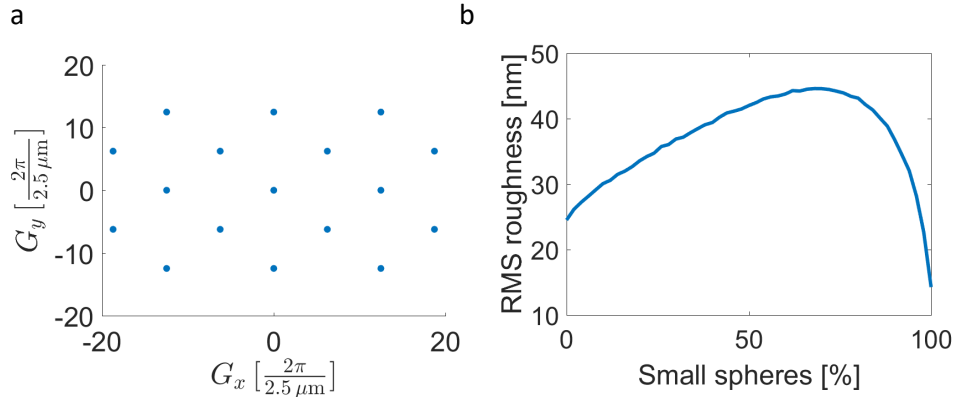
a

b

Fig. 4. a) Diffraction pattern of an ideal hexagonal monolayer of single-sized nanospheres with radius of 170 nm. The blue dots indicate the available discrete diffraction channels. b) Average root mean square (RMS) roughness of a surface consisting of nanospheres with 170 nm radius and an increasing portion of nanospheres with 120 nm radius. The graph shows the average of 20 generated height profiles for each portion of larger and smaller nanospheres in steps of 2 %. By increasing the portion of the small nanospheres, the RMS roughness first increases up to a portion of approx. 70 % of nanospheres, before it quickly drops; this is due to smearing out of the surface features accompanying the diminishing influence of the bigger nanospheres.

$$\text{PSD}(\vec{G}) = \frac{1}{L_x L_y} \left| \sum_m \sum_n h(x_m, y_n) e^{-\mathrm{i}(G_x^m x_m + G_y^n y_n)} \Delta L^2 \right|^2 . \tag{1}$$

L_x and L_y are the considered widths of the rough surface in x and y direction and G_x^m and G_y^n are the spatial frequencies in x and y direction that belong to the diffraction orders m and n, respectively. ΔL is the minimal step width of the generated discrete height profile. Due to the discreteness of the transformation, G_x^m (and similarly G_y^n) can also be written as $G_x^m = \frac{2\pi}{L_x} m$. As an example, Fig. 4(a) shows the PSD of a hexagonal sinusoidal grating. The PSD must be calculated for a simulation window much larger than the correlation length of the disordered structure to ensure statistical significance and stability of the Fourier distribution [44].

In general, the PSD is a useful predictor for the diffraction efficiency in the limit of shallow textures [11], meaning that the wavelength incident to the rough surfaces is much larger than the amplitude modulation of the texture. For our setup, the wavelength in c-Si is, assuming a vacuum wavelength of 700 nm, approximately 185 nm. A measure for the strength of the amplitude modulation is the root mean-square (RMS) roughness, shown in Fig. 4(b) for the nanosphere size combination 170 nm and 120 nm and increasing portion of the 120 nm sized nanospheres. The RMS roughness almost doubles its value up to around 45 nm when small nanospheres are gradually added, which is only around four times smaller than the wavelength. This suggests that the PSD prediction will be less reliable in such conditions when the portion of the two nanosphere sizes are almost the same.

Even with a dense nanosphere monolayer comprising of only identical nanospheres, one can already obtain an annulus-like shaped distribution when a disordered placement is allowed. Figure 5(a) shows the PSD profile of a surface texture consisting of one nanosphere size species. The PSD profile was made for a $10 \times 10 \ \mu\text{m}^2$ for the case of a $r_{\text{main}} = 170$ nm. The nanosphere
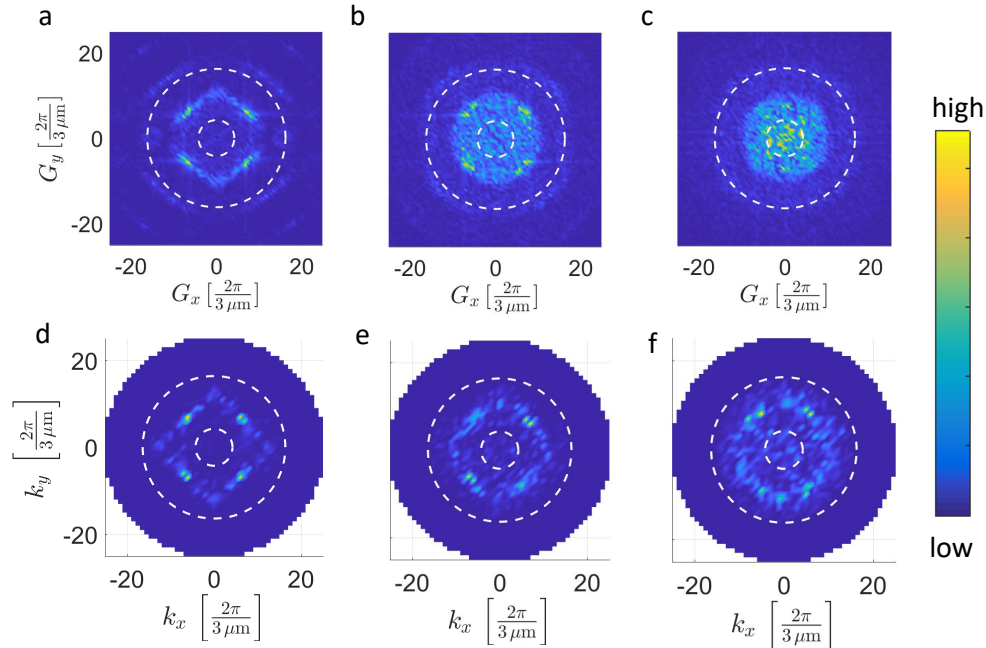
Fig. 5. Plots of the PSD (5(a)–5(c)) and the diffracted angular spectra (5(d)–5(f)) at a wavelength of 700 nm for three different portions of small nanospheres. The white dashed rings mark the annulus sketched in Fig. 1(b) with optimized inner and outer radius. Figures 5(a)–5(c) show PSD plots of disordered monolayers where the radius of the main nanosphere species is $r_{main} = 170$ nm and the perturbing nanospheres have $r_{pert} = 120$ nm, and Figs. 5(d)–5(f) show diffraction plots of such monolayer configurations, respectively. For the PSD plots, the average height of the height profiles was set to zero to remove the zeroth order component, and in the diffraction plots, the zeroth order is not shown. Percentages of the perturbing nanospheres are: a, d: 0%; b, e: 10%; and c, f: 40%. For the small perturbations of 0% and 10%, the PSD and diffraction components are mainly located centrally in the previously defined annulus region, whereas for higher perturbations, the PSD pattern transforms into a disk.

radius determines both the amplitude of the height profile and the average correlation length, which in turn affects the scattering strength and the Fourier components that are populated. Smaller radii lead to surface textures with weaker scattering strength but populate Fourier components with large $|\vec{G}|$, while larger radii lead to stronger scattering strength but more population of Fourier components at smaller $|\vec{G}|$. Choosing the radius $r_{main} = 170$ nm is not based on a systematic analysis, it is merely a plausible choice taking into account the previously discussed requirements of the height profile. The choice can be motivated by the fact that it leads to a population of the Fourier distribution in our target Fourier annulus region in the spectral region of interest. Furthermore, this radius indeed provides strong scattering in the directions and wavelength range of interest reaching around 74% as will be shown below. By having placement disorder while maintaining a dense arrangement, one actually observes a ring-shaped broadening (cf. Fig. 5(a)) of the main peaks of the Fourier distribution compared to a purely ordered system. Allowing placement randomness thus already promises to provide significant boost to light trapping.

To ensure a spectrally broadband enhancement effect, one of course is interested in broadening the ring-like spectra. One can further broaden the annulus-shaped Fourier distribution obtained

by allowing another nanosphere size species to generate the monolayer. A similar strategy was chosen in [45], where two different sphere sizes have been used to engineer the light propagation in a photonic glass. Interestingly, by just considering a distribution of two nanosphere sizes, one can already obtain a sufficiently broad annulus-like distribution of surface texture Fourier components as demonstrated in Figs. 5(b) and 5(c) when another nanosphere size species is successively introduced in the monolayer. Naturally, as the amount of the other nanosphere size species is increased, the PSD profile is also populated at low $|\vec{G}|$ where scattering would be near-normal. The second nanosphere size species is considered to have a radius $r_{\mathrm{pert}} = 120$ nm. The motivation to use a smaller nanosphere size is to avoid a PSD profile that is too dominant at low $|\vec{G}|$ which would naturally occur if bigger nanospheres are added.

A large PSD in the annulus region would not itself guarantee that also the scattering strength is stronger in the annulus, as also only the available number of scattering channels could be increased. When additionally looking at the RMS roughness in Fig. 4(b) when increasing the portion of perturbing small nanospheres, we can settle this question. By increasing the portion of small nanospheres, the RMS roughness starts from 24 nm for no perturbing nanospheres added and increases up to 44 nm for 68% of small nanospheres; for higher portions of small nanospheres, the RMS roughness will go down again. These values compare to the RMS roughness value of Asahi-U profiles, which have a RMS roughness of 35 nm [11]. The RMS roughness is a measure of how strong a surface scatters, but does not specify the angular frequencies at which this happens. But together with the PSD, we can conclude that by adding perturbing small nanospheres, we increase the total scattering strength in the target annulus region, as we intended.

To confirm the scattering properties, we calculate the scattering of normal incident waves impinging on a c-Si/Ag textured interface with the commercial FEM solver JCMsuite [46]. Our simulation domain for the diffraction calculations essentially consists only of the dashed box region in Fig. 1(a) with only the real part of the refractive index of c-Si considered. The surface texture is assumed to be transfered perfectly to an Ag substrate. In practice, one can achieve the same effect by applying a metal coating on the nanosphere monolayers. If the metal coating is thick enough, the fact that the nanospheres themselves are made of a dielectric material can be neglected. Jäger *et al.* demonstrated that one can obtain a statistically meaningful result when modeling the scattering property of a disordered texture by considering a periodified cut of the domain that spans at least five times the lateral feature size (LFS) [44]. In our case, the LFS, in a good approximation, can be considered to be the distance between two nanospheres with the same radius of the prevalent nanosphere species. For portions of the larger nanospheres between 50% and 100%, this means that $LFS \approx 2r_{\mathrm{main}} = 340$ nm. If the smaller nanospheres are the dominant portion, $LFS \approx 240$ nm. We choose the computational domain size to be at least $2.5 \times 2.5 \ \mu\mathrm{m}^2$, which is around seven times larger than the LFS. Hence, statistical validity of our results is ensured.

Figures 5(d)–5(f) show the angular distribution of the diffraction efficiency at a wavelength of 700 nm. As can be seen in Figs. 5(a) and 5(d), the diffraction efficiency follows well the PSD profile for the case of identical nanospheres in the monolayer. As the percentage of small nanospheres is increased, the annulus in the diffraction profile broadens. It is also noticeable that the diffraction still preserves its annulus shape while the PSD completely turns into a disk as the two portions of the nanosphere size species are becoming equal. This indicates that the diffraction, even when considering larger fraction of the small nanospheres, continues to be determined by the larger nanospheres; the smaller nanospheres only act as a perturbation by broadening the annulus.

Despite discrepancies between the diffraction efficiency and PSD($\vec{G}$) displayed in Fig. 5, we found that the integration of the PSD($\vec{G}$) within the target annulus region is still a useful figure of merit to predict the absorption enhancement capability. To be more exact, this figure of merit is defined by
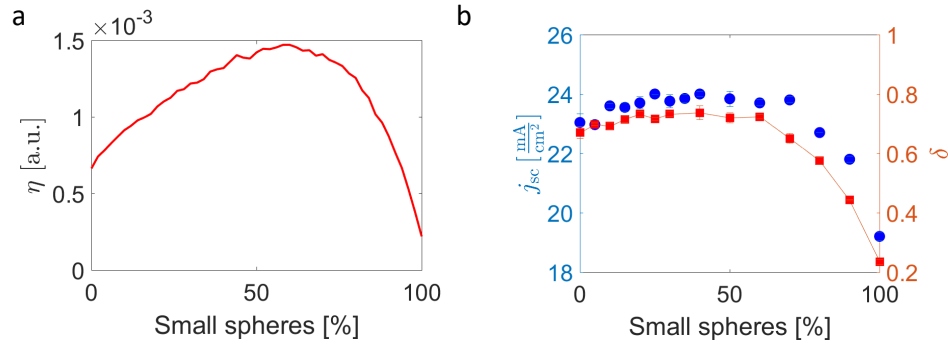
Fig. 6. Comparison between the contributions of the PSD and the diffraction components, both summed up in the annulus region B indicated in Fig. 1(b). a) By increasing the portion of the small nanospheres, the sum of the PSD components in the annulus (η) doubles its value up to around 60 % of small nanospheres due to the introduction of more Fourier components by the perturbing nanospheres, and then decreases rapidly as the smaller nanospheres generate a less rough surface morphology. b) The diffraction efficiency in the annulus (δ, red squares) shows the same tendency, but with a less pronounced peak. The short-circuit current density j_{sc} (blue dots) shows a similar behavior with a peak at around 50 %. The increase of j_{sc} from 0 % to 50 % amounts to 1.1 $\frac{\text{mA}}{\text{cm}^2}$. Each datapoint of η is the average of three simulations, and each j_{sc} datapoint is the average of at least two simulations. The error bars indicate the uncertainty of the averages.

$$\eta = \sum_{\substack{G_x^m, G_y^n, \\ k_{\text{TIR}} < G_{||} < k_{\text{inc}}}} \text{PSD}(G_x^m, G_y^n), \tag{2}$$

where $G_{||} = \sqrt{(G_x^m)^2 + (G_y^n)^2}$ is the in-plane spatial frequency for diffraction channel (m, n). The formula states that those components of the PSD are summed up which fulfill the criterion that the in-plane spatial frequency lies in the interval between the wavevector of total internal reflection and the largest non-evanescent mode. This interval, as discussed before, is most beneficial for light-trapping purposes.

Figure 6(a) depicts a plot of η versus the portion of smaller nanospheres in the monolayer. η was calculated for 20 iterations of the same size fraction of the nanospheres in steps of 2 %. A distinct peak around 60% of smaller nanospheres is seen. The dependency of the figure of merit η on the percentage of smaller nanospheres is comparable to the diffraction efficiency δ within the annulus region, calculated by

$$\delta = \sum_{\substack{k_x^m, k_y^n, \\ k_{\text{TIR}} < G_{||} < k_{\text{inc}}}} |\vec{E}_{\text{ref}}(k_x^m, k_y^n)|^2 \frac{k_z}{k_{\text{inc}}}, . \tag{3}$$

Here, $\vec{E}_{\text{ref}}(k_x^m, k_y^n)$ is the spectral representation of the reflected field above the surface, and it is implicitly assumed that the incident field has a unit magnitude so that the normalization factor in δ can be omitted. δ hence gives the portion of the total diffraction efficiency which goes into the target region.

Figure 6(b) (red squares) gives the plot of integrated diffraction efficiencies versus the portion of the small nanospheres. Every datapoint is the average of at least three simulations using

different height profiles with the same fraction of nanosphere sizes. The red line in Fig. 6(b) is a guide to the eye. A common trend can be seen with a broad plateau peak at small nanosphere percentages between around 30 % and 60 %. The observation that the diffraction is relatively insensitive for the perturbing nanospheres in this percentage regime indicates that the degree of disorder does not change much for these percentages; having 30 % perturbing small nanospheres and adding another 10 % does neither further broaden the diffraction spectrum nor decrease the scattering strength of the available Fourier components.

2.4. Full-wave simulations

To validate the performance of our textures, we proceed to calculate the impact of the different textures on the absorption in the c-Si thin-film solar cell stack shown in Fig. 1(a). We consider a solar cell structure with a silver back reflector, 1 μm thick c-Si absorber layer, and a 50 nm thick anti-reflection layer (Indium tin oxide, ITO [42]). This multilayer structure is not supposed to be realized experimentally exactly in this scheme, as a corrugated back surface and a flat front surface are hard to achieve with current techniques and we are also omitting the usually used TCO layer between the metal back reflector and the c-Si layer. However, for our purposes of providing a strategy for optimizing the rough back reflector, it is sufficient: The TCO layer would not significantly influence the diffraction properties and a textured front side of the cell would narrow down the applicability of the analyses compared to just a flat front side.

Our simulation domains vary in size, but are at least 2.5 μm by 2.5 μm large to ensure statistically stable results. We simulate for the absorption between 300 nm and 1100 nm in steps of 10 nm with normal incident plane waves.

The macroscopic quantity of interest is the short-circuit current density j_{sc}. To obtain j_{sc}, we calculated the absorption in the silicon layer by integrating the divergence of the Poynting vector over the volume of the c-Si layer using JCMsuite:

$$A(\lambda) = \int_V \vec{\nabla} \cdot \vec{S}(\lambda) \, dV \, . \tag{4}$$

The short-circuit current density is afterwards calculated by weighting the absorption efficiency with the solar cell spectrum [10]:

$$j_{sc} = e \int_{300\text{nm}}^{1100\text{nm}} \text{QE} \cdot A(\lambda) \cdot \phi(\lambda) \, d\lambda \, . \tag{5}$$

$\phi(\lambda)$ is the AM 1.5G solar irradiation photon number spectrum [47], e is the elementary charge, and we further assume optimal photon conversion into electrons and holes, thus the quantum (i.e. collection) efficiency $QE = 1$.

Comparing the sum of all PSD components in the annulus (Fig. 6(a)) with the diffraction components in the annulus (red squares in Fig. 6(b)), we see that both quantities follow the same trend, but the slopes and the pronounciation of the peaks are considerably different. Beginning at 0 % small nanospheres, the components in the annulus increase slowly when the portion of small nanospheres is increased since more Fourier components caused by the perturbing nanospheres do emerge. The zeroth order (not shown) will, at the expense of the annulus components, decrease as the roughness of the surface is increased. At around 50 %, the integrated diffraction efficiency δ reaches a plateau. This plateau can also be seen in the short-circuit current density (blue dots in Fig. 6(b)), whereas the PSD contributions still increase up to a portion of 60% small nanospheres. The trend in the short-circuit current density thus follows closely the trend seen in the integrated diffraction efficiency at 700 nm. The uncertainty from three diffraction simulations at each datapoint is very small; insofar, we can conclude that for obtaining values for the short-circuit current density with low uncertainties, only a few simulations are needed also.

A 1 μm thick c-Si layer on top of a flat silver substrate and with a 50 nm ITO layer yields a short-circuit current density of $j_{sc} = 15.3 \frac{mA}{cm^2}$. For the same stack with a backreflector made from a hexagonally ordered monolayer with one nanosphere size species with radius 170 nm, the short-circuit current density is $j_{sc} = 21.1 \frac{mA}{cm^2}$. For the disordered case (but still retaining only one nanosphere size), the average short-circuit current density amounts to 23.0 $\frac{mA}{cm^2}$. This means that the relative increase of the short-circuit current density by giving up the hexagonal order amounts to 9 %. Introducing perturbing nanospheres will then increase the short-circuit current density even more. It is apparent from Fig. 6(b) that the short-circuit current density exhibits a similar dependency trend as the diffraction efficiency at 700 nm. Though the latter one is more expensive to calculate than the PSD, it is, at least for the height profiles considered here, a better predictor of the short-circuit current density increase than the PSD. Nevertheless, due to the fast availability of the PSD for a large number of height profiles, the PSD still can be used as a first guess for the target nanosphere size distribution.

We observe from our simulations a maximum value of $j_{sc} = 24.1 \frac{mA}{cm^2}$ at a portion of 60 % perturbing nanospheres. This is an enhancement of 58 % compared to the flat surface, 13.7 % compared to the hexagonal ordered surface and 4.8 % compared to the single nanosphere-size case without order. The uncertainty of the short-circuit current density values for the disordered cases is of the order of 0.1 $\frac{mA}{cm^2}$, which indicates that the results are statistically stable.

3. Summary and conclusions

We present a strategy how one can reliably obtain a favorable light-trapping surface texture from a bottom-up fabrication approach based on colloidal nanospheres. The generated surface texture can be ensured to possess an optimal Fourier distribution for light trapping, by having a relatively simple nanosphere size distribution comprising of only two radii. An annulus shaped Fourier spectrum, which favors scattering to oblique angles in the target wavelength range for enhancement, is obtained. We discuss how analyzing the Power Spectral Density of the height profile generated from a monolayer of identical nanospheres can give guidance in choosing the nanospheres' radii. We show that the diffraction efficiency in the target wavelength range for light trapping is a better predictor for the optimum nanosphere monolayer parameters than the PSD.

We proceed to demonstrate the application of such surface textures in a thin-film c-Si cell, and obtained a short-circuit current density enhancement of 13.7 % compared to the hexagonal ordered surface and 4.8 % compared to the disordered single nanosphere-size monolayer. Further optimization of the radius choice is still possible and promises an even stronger short-circuit current enhancement. This work opens the possibility to obtain a highly efficient light trapping structure in a technology that is directly ready for upscaling in a cost effective manner.

Disclosures

The authors declare that there are no conflicts of interest related to this article.